

Research paper

Analytical solution of unsteady heat conduction in multilayer internal combustion engine walls

G. Koutsakis*, J.B. Ghandhi

Engine Research Center, University of Wisconsin–Madison, Madison, WI, 53706, United States of America

ARTICLE INFO

Keywords:

Thermal barrier coating
Temperature swing
Heat flux
Internal combustion engine
Heat conduction
Drive cycle

ABSTRACT

An analytical solution of the unsteady heat conduction problem in multilayer walls was developed and applied to study thermal barrier coatings for reciprocating internal combustion engines. The mathematical solution was derived using the matrix method and complex analysis/residue-calculus Laplace transform inversion techniques. The one-dimensional domain includes a time-varying heat flux on the combustion chamber surface, and a time-varying temperature on the backside coolant surface. These boundary conditions are simulated as the superposition of two adjacent triangular, unit-magnitude pulses, which gives a piece-wise linear representation of the applied flux or temperature history. The temperature at any location of interest is found as the convolution of the transfer function, which results from the inversion, with the discrete-time heat flux or backside temperature history. The transfer functions describe the exact response and only depend on multilayer architecture, therefore, they can be computed *a priori*. The triangular pulse method provides a more than two order of magnitude reduction in computation time compared to a finite difference solution at the same level of accuracy. A 10^4 -fold speed increase relative to a finite difference solution was realized when using the Overlap-add convolution technique for a full drive cycle simulation, *i.e.*, a long time record. The surface response or transfer function acts like a finite impulse response and can be viewed in the frequency domain to reveal complementary information about coating performance.

1. Introduction

Internal combustion engines manufacturers are under pressure to increase thermal efficiency, reduce exhaust gas pollutant emissions, and maintain high power density. The latter involves higher cylinder pressures and, therefore, the combustion chamber surfaces tend to run hotter. Thermal barrier coatings provide a path to restrain metal temperature and reduce thermal losses. There is significant interest in the application of thin, low thermal conductivity, k , and low volumetric heat capacity, ρc , coatings because they can follow the gas temperature swings closely and, thus, reduce the gas-wall temperature difference that drives heat transfer to the chamber surfaces.

Research on the insulation of reciprocating engine surfaces with coatings has been ongoing for almost 45 years. The historical evolution of thermal barrier coating technology for this application is provided in a recently published literature review [1] that focused on the performance and emission characteristics associated with in-cylinder heat insulation. It is clear that a general framework to describe the unsteady heat conduction of reciprocating engine coatings is still needed.

Finite difference methods are the conventional approach employed to determine the coating surface dynamic temperature. Explicit

schemes [2–4] are simple and computationally efficient, but, they become unstable above a critical time step. The relatively short thermal conduction time scale of the coating together with high temporal gradients of heat flux at the surface require high nodal density near the coating surface to guarantee numerical stability and accuracy. Implicit schemes [5–7] are unconditionally stable and handle non-uniform grid spacing, but, can require large matrix inversions, which may become computationally costly when such calculations are coupled with combustion engine simulations. Guaranteed stability, however, does not eliminate the possibility of oscillations, so there are still limits on the time step size. A number of surrogate procedures have been used to compensate for computational cost. For the 1-D approach, commercial codes have assumed constant temperature at the coating–substrate interface during the cycle. However, this treatment may not conserve energy for cases where the temperature at that location fluctuates [6]. Some researchers have attempted to couple 3-D CFD simulations and low spatial resolution heat conduction calculations, where the material properties near the surface were chosen to minimize errors in the dynamics of the system [8–10]. Lastly, the finite difference schemes require the entire temperature distribution to be evaluated at

* Corresponding author.

E-mail address: koutsakis@wisc.edu (G. Koutsakis).

Nomenclature

\dot{q}''	Heat flux [W m^{-2}]
\bar{q}''	Mean heat flux [W m^{-2}]
h	Heat transfer coefficient [$\text{W m}^{-2} \text{K}$]
t	Temperature [K]
θ	Time [s]
Δ	Time step [s]
X	Combustion chamber response function subject to heat flux pulses [$\text{K m}^2 \text{W}^{-1}$]
Y	Coolant surface response function subject to backside temperature pulses [-]
k	Thermal conductivity [$\text{W m}^{-1} \text{K}^{-1}$]
ρ	Density [kg m^{-3}]
c	Specific heat capacity [$\text{J kg}^{-1} \text{K}^{-1}$]
ρc	Volumetric heat capacity [$\text{J m}^{-3} \text{K}^{-1}$]
x	Distance [m]
L	Length [m]
A, B, C, D	Matrix coefficients
N	Number of layers [-]
R	Thermal resistance [$\text{m}^2 \text{K W}^{-1}$]
C	Capacitance per unit area [$\text{J m}^{-2} \text{K}^{-1}$]
s	Laplace, frequency variable [Hz]
β	Positive real number and simple root of $D(s)$ [Hz]
Ψ	Generalized residue
ψ	Generalized residue parameter
n_x, n_y	Summation terms
Ω_m	Root dependent ratio
$f()$	Function of ()
\mathcal{F}	Fast Fourier transform operation
\mathcal{F}^{-1}	Inverse fast Fourier transform operation
r	Magnitude of complex function

Subscripts

g	Gas
w	Wall
c	Coolant
u	Upstream
d	Downstream
i	Surface/interface index
m	Root index
j, n	Time index
ini	Initial
N	Coolant-side surface
o	Combustion chamber surface
rad	Radiation

every time step; quite often the surface temperature is the only output of interest explicitly for providing boundary conditions to an engine simulation.

Existing approaches to conjugate heat transfer with combustion solvers are computationally expensive. However, because coating optimization may require evaluation over a wide range of material architectures and engine conditions, computational efficiency is critical. The coating effectiveness varies based on operating condition due to the non-linear coupling in an engine. In order to provide a comprehensive comparison between different coating designs, one needs to consider extended operation periods, *i.e.* drive cycles [11]. An analytical solution is more appropriate to evaluate heat conduction because (i) it is exact,

conv Convection

Abbreviations

⊗	Convolution symbol
TBC	Thermal Barrier Coating
YSZ	Yttria Stabilized Zirconia
CPU	Central Processing Unit
FFT	Fast Fourier Transform
EGR	Exhaust Gas Recirculation
ECU	Electronic Control Unit

(ii) does not depend on spatial discretization; (iii) it is computationally efficient since it solves for the only output of interest.

These authors [12] have developed an analytical approach to determine surface temperature subject to a time-varying heat flux. The applied heat flux was approximated as a series of step-changes; the backside temperature was held constant. A special case solution of the two-layer wall (coating and substrate) problem provided the foundation for defining a set of non-dimensional parameters that uniquely characterize the surface temperature swing for arbitrary periodic heat flux. The non-dimensional parameters have been exploited to identify thermodynamically equivalent materials suitable for conjugate heat transfer applications. A thicker layer of this pseudo-material matches the dynamics and allows lower resolution (more efficient) conjugate heat transfer simulations [9].

The objective of this work is to provide an improved analytical solution to the transient heat conduction problem of thermal barrier coatings in reciprocating internal combustion engines. The current technique provides a solution to the problem of both domain-end boundary conditions being functions of time and approximates the applied boundary conditions as a series of triangular pulses that combine to give a piece-wise linear approximation. Transfer functions are derived for any interface location, not just the surface, and rely only on the material architecture, *i.e.* material thermal properties and thickness. The analytical approach is developed in the following section. The framework is then demonstrated for a simplified scenario followed by an evaluation of all interface temperature histories for a full drive cycle, with an emphasis on assessing the computational efficiency. Finally, surface responses are explored in the frequency domain to provide a comprehensive understanding of the coating performance.

2. Surface temperature subject to unsteady combustion chamber surface heat flux and backside surface temperature

2.1. Problem setup

Consider 1-D heat flow in a multilayer engine wall with overall thickness L and constant thermophysical properties within each layer. The governing heat diffusion equation is

$$k \frac{\partial^2 t}{\partial x^2} = \rho c \frac{\partial t}{\partial \theta} \quad (1)$$

where t is temperature, θ is time, x is location, k and ρc are thermal conductivity and volumetric heat capacity, respectively. The $x = 0$ location represents the combustion chamber surface where a time-varying heat flux, $\dot{q}''_o(\theta)$, is imposed

$$-k \frac{\partial t}{\partial x} \Big|_{x=0} = \dot{q}''_o(\theta) = f(\theta) \quad (2)$$

The applied heat flux is unsteady and can be aperiodic during transient operation of a reciprocating engine.

During startup or engine load changes the back side of the wall may show significant temperature changes due to, for example, the coolant

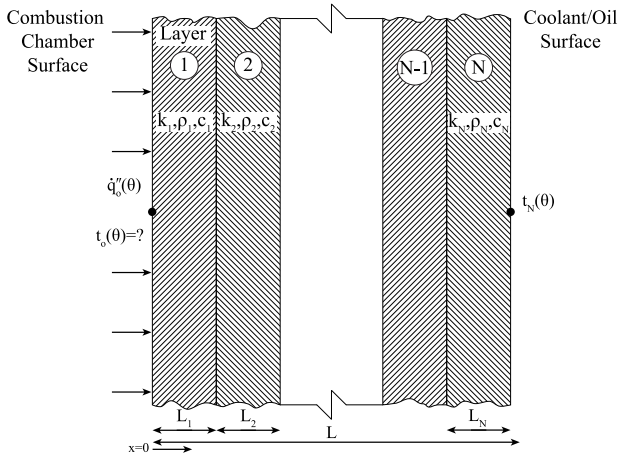


Fig. 1. Illustration of an 1-D multilayer engine wall. Both boundary conditions, i.e. heat flux on the combustion chamber gas-side and temperature on the coolant side, are prescribed functions of time.

heating. The backside condition at $x = L$, the coolant or oil surface, is therefore also allowed to vary as a prescribed function of time

$$t_N(\theta) = f(\theta) \quad (3)$$

The transient heat conduction problem is formulated with linear and homogeneous boundary conditions. The thermophysical properties vary only with spatial domain.

The problem is divided into four sub-problems and their superposition comprises the general solution [13]. The first and second problems are comprised from the time-varying heat flux at the combustion surface and the time-varying backside temperature at the coolant/oil surface, respectively, as shown in Fig. 1. The third and fourth sub-problems address the initial conditions associated with the prior combustion chamber heat flux and coolant-side surface temperature, respectively.

2.2. Unit triangular pulse

In engine heat transfer, the boundary conditions are not known as a continuous function. Rather, temperature or heat flux data are provided only in a discrete fashion from a numerical solution. The boundary conditions can be approximated as sequential step changes [12] or straight-line interpolation. It has been shown that linear interpolation is equivalent to the sum of triangular pulses and offers the highest possible accuracy [14–16].

Heat flux and temperature signals contain a large number of frequency components. Fig. 2 shows how an ideal continuous function is approximated as discrete via the step-change and linear interpolation approximation methods. It is clear that the step function approximation method would require smaller time steps than the linear interpolation method to give the same accuracy. In the linear interpolation approximation method, two adjacent triangular time-based pulses (shown with red dashed lines) are overlapped to form a trapezoidal pulse (straight red line) of width Δ .

A triangular pulse is built from three time-interval ramp functions, as shown in Fig. 3,

$$\begin{aligned} p(\theta_n) &= 0, & \text{for } \theta_n \leq 0 \\ &= y_1 = \frac{\theta_n}{\Delta}, & \text{for } 0 < \theta_n \leq \Delta \\ &= y_1 + y_2 = 2 - \frac{\theta_n}{\Delta}, & \text{for } \Delta < \theta_n \leq 2\Delta \\ &= y_1 + y_2 + y_3 = 0, & \text{for } \theta_n > 2\Delta \end{aligned} \quad (4)$$

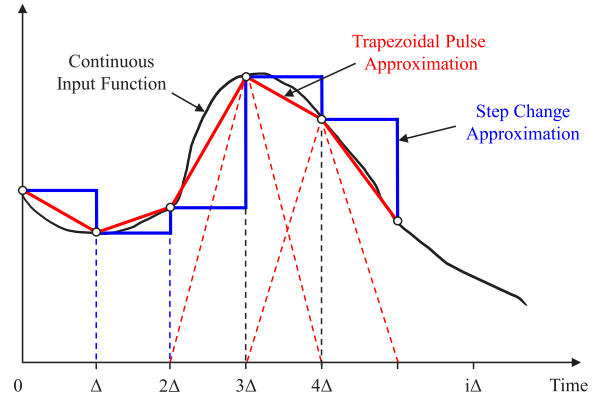


Fig. 2. Representation of a continuous (black) boundary condition input as successive step changes (blue) and the sum (solid red) of two trapezoidal pulses (dashed red), shown on a time step Δ basis.

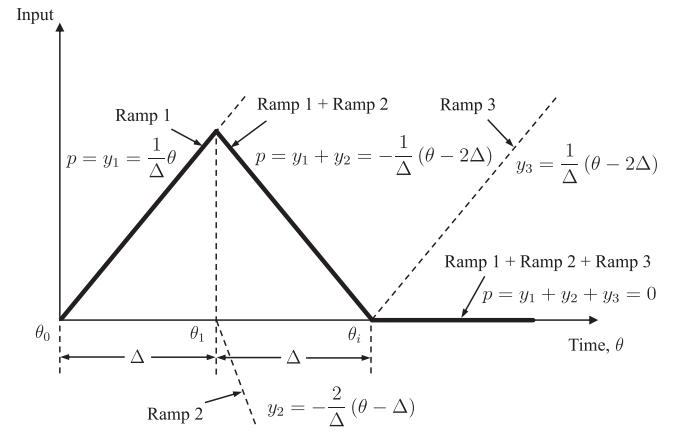


Fig. 3. Unit triangular pulse composed of three time-based ramp functions [15].

The Laplace transform of $p(\theta_n)$ is given by

$$\begin{aligned} \hat{p}(s) &= \frac{1}{\Delta s^2}, & \text{for } 0 < \theta_n \leq \Delta \\ &= \frac{1}{\Delta s^2} (1 - 2e^{-s\Delta}), & \text{for } \Delta < \theta_n \leq 2\Delta \\ &= \frac{1}{\Delta s^2} (1 - e^{-s\Delta})^2, & \text{for } \theta_n > 2\Delta \end{aligned} \quad (5)$$

where s is the Laplace transform variable.

2.3. Residue-calculus Laplace transform inversion

Using the notation \hat{t}_o is the Laplace transform of the gas-side surface temperature, and likewise \hat{q}_o is the Laplace transform of the combustion-chamber surface heat flux, one can write for an engine wall composed of any number of layers

$$\begin{bmatrix} \hat{t}_o \\ \hat{q}_o \end{bmatrix} = \begin{bmatrix} A & B \\ C & D \end{bmatrix} \begin{bmatrix} \hat{t}_N \\ \hat{q}_N \end{bmatrix} \quad (6)$$

where N is the number of layers and \hat{t}_N and \hat{q}_N are the transform of t and q'' at the coolant/oil surface. The coefficients of the matrix in Eq. (6) define the overall transfer matrix that is comprised of the product of transfer matrices of each individual layer

$$\begin{bmatrix} A & B \\ C & D \end{bmatrix} = \begin{bmatrix} A_1 & B_1 \\ C_1 & D_1 \end{bmatrix} \cdot \begin{bmatrix} A_2 & B_2 \\ C_2 & D_2 \end{bmatrix} \cdots \begin{bmatrix} A_N & B_N \\ C_N & D_N \end{bmatrix} \quad (7)$$

The transfer matrix for each layer is given by [17]

$$\begin{bmatrix} A_i & B_i \\ C_i & D_i \end{bmatrix} = \begin{bmatrix} \cosh \sqrt{s R_i C_i} & \frac{R_i}{\sqrt{s R_i C_i}} \sinh \sqrt{s R_i C_i} \\ \frac{\sqrt{s R_i C_i}}{R_i} \sinh \sqrt{s R_i C_i} & \cosh \sqrt{s R_i C_i} \end{bmatrix} \quad (8)$$

where $R_i = L_i/k_i$ and $C_i = L_i \rho_i c_i$ are the thermal resistance and volumetric heat capacity per unit area of layer i , respectively.

The overall equation for the multilayer wall is recast in a manner that exploits the known boundary conditions \hat{t}_N and \hat{q}_o

$$\begin{bmatrix} \hat{t}_o \\ \hat{q}_N \end{bmatrix} = \frac{1}{D} \begin{bmatrix} 1 & B \\ -C & 1 \end{bmatrix} \begin{bmatrix} \hat{t}_N \\ \hat{q}_o \end{bmatrix} \quad (9)$$

The combustion surface temperature transform, subject to transient combustion heat flux and coolant temperature, is

$$\hat{t}_o = \left(\frac{B}{D}\right) \hat{q}_o + \left(\frac{1}{D}\right) \hat{t}_N \quad (10)$$

and must be inverted from the frequency to time domain using the Laplace transform residue-calculus inversion technique.

The two terms in Eq. (10) share a common denominator, D ; the numerator includes the triangular pulse \hat{p} , since $\hat{q}_o = \hat{p} \cdot q_o$ and $\hat{t}_N = \hat{p} \cdot t_N$, scaled by either B (heat flux) or unity (back-side temperature), and can be cast as

$$\Psi = \left(\frac{\hat{p}\Psi}{D}\right) \quad (11)$$

Utilizing the general formula of the inverse Laplace transform, one gets

$$\mathcal{L}^{-1}\{\Psi\} = \frac{1}{2\pi j} \int_{\gamma-j\infty}^{\gamma+j\infty} \Psi \cdot e^{s\theta} ds \quad (12)$$

where $j = \sqrt{-1}$ and the constant γ is a large positive real number approaching infinity. Inverse transforms of this kind are neither listed in standard tables nor given by computer software packages (even for a relatively simple two-layer problem). The residue theorem provides a powerful tool to evaluate integrals such as Eq. (12) as the sum of the residues at the poles of Ψ . A complete derivation of an inversion for the step-change input solving only the transient combustion chamber heat flux can be found in [12] along with an analytical solution for the limit of negligible coating thermal inertia.

Following the same approach,

$$\mathcal{L}^{-1}\{\Psi\} = \text{Res}(\Psi; 0) + \sum_{m=1}^{\infty} \text{Res}(\Psi; -\beta_m) \quad (13)$$

where the first term arises from singularities at $s = 0$, and the second term represents the residues at the poles $s = -\beta_m$.

There is a double pole at $s = 0$ when the triangular approximation is used. Using Eq. (5) the residue is given by

$$\begin{aligned} \text{Res}(\Psi; 0) &= \left[\frac{\Psi}{D}\right]_{s=0} + \frac{1}{\Delta} \frac{d}{ds} \left[\frac{\Psi}{D}\right]_{s=0}, \text{ for } 0 < \theta_n \leq \Delta \\ &= -\frac{1}{\Delta} \frac{d}{ds} \left[\frac{\Psi}{D}\right]_{s=0}, \text{ for } \Delta < \theta_n \leq 2\Delta \\ &= 0, \text{ for } \theta_n > 2\Delta \end{aligned} \quad (14)$$

The second term of the right-hand side of Eq. (13) represents the summation of all residues that lie on the negative real axis [12]. Finding the pole locations β_m requires numerical evaluation because $D(s) = 0$ becomes transcendental for walls with more than a single layer [12,18]. The residues at $s = -\beta_m$ are

$$\begin{aligned} \text{Res}(\Psi; -\beta_m) &= \Omega_m \cdot e^{-\beta_m \Delta}, \text{ for } 0 < \theta_n \leq \Delta_0 \\ &= \Omega_m \cdot (1 - 2e^{\beta_m \Delta}) \cdot e^{-2\beta_m \Delta}, \text{ for } \Delta < \theta_n \leq 2\Delta \\ &= \Omega_m \cdot (1 - e^{\beta_m \Delta})^2 \cdot e^{-i\beta_m \Delta}, \text{ for } \theta_n = n\Delta > 2\Delta \end{aligned} \quad (15)$$

where

$$\Omega_m = \frac{\Psi(s)|_{s=-\beta_m}}{\Delta \beta_m^2 \frac{dD}{ds}|_{s=-\beta_m}} \quad (16)$$

The inverse functions $X(\theta) = \mathcal{L}^{-1}\{\Psi(\psi = B)\}$ and $Y(\theta) = \mathcal{L}^{-1}\{\Psi(\psi = 1)\}$ at discrete times $\theta_n = n\Delta$ ($n = 0, 1, 2, \dots$) for unit magnitude of p are found by evaluating (13) with (14) and (15)

$$\begin{aligned} X_i(\theta_o) \text{ or } Y_i(\theta_o) &= \left[\frac{\Psi}{D}\right]_{s=0} + \frac{1}{\Delta} \frac{d}{ds} \left[\frac{\Psi}{D}\right]_{s=0} \\ &+ \sum_{m=1}^{\infty} \Omega_m \cdot e^{-\beta_m \Delta}, \text{ for } n = 0 \end{aligned} \quad (17)$$

$$\begin{aligned} X_i(\theta_1) \text{ or } Y_i(\theta_1) &= -\frac{1}{\Delta} \frac{d}{ds} \left[\frac{\Psi}{D}\right]_{s=0} \\ &+ \sum_{m=1}^{\infty} \Omega_m \cdot (1 - 2e^{\beta_m \Delta}) \cdot e^{-2\beta_m \Delta}, \text{ for } n = 1 \end{aligned}$$

$$X_i(\theta_i) \text{ or } Y_i(\theta_i) = \sum_{m=1}^{\infty} \Omega_m \cdot (1 - e^{\beta_m \Delta})^2 \cdot e^{-(n+1)\beta_m \Delta}, \text{ for } n = 2, 3, \dots$$

where the subscript $i = 0$, refers to the combustion chamber surface. The full solution for t_o using the time-dependent X_o and Y_o responses will be discussed below.

The values of B , D , $\frac{dB}{ds}$ and $\frac{dD}{ds}$ need to be known at $s = 0$ and $s = -\beta_m$ ($m = 1, 2, \dots$) where β_m are the roots of D , i.e., $D(s = -\beta_m) = 0$, which lie on the negative real-axis as shown by Carslaw and Jaeger [13]. The transfer matrix and its analytical derivative with respect to the frequency variable can be found in Appendix A.

Multilayer walls result in transcendental characteristic equation $D(s) = 0$ that must be solved numerically. The root-finding algorithm involves scanning between the range $0 < \beta \leq \beta_{\max}$, where the value of cut-off frequency β_{\max} can be estimated. The contribution of the β_{\max} term to X or Y is at most $e^{-\beta_{\max} \Delta}$ where Δ is the time step. To ensure a precision of 5×10^{-5} , for example, one can safely neglect the contribution from those roots for which $e^{-\beta_{\max} \Delta} < 5 \times 10^{-5}$ or $\beta_{\max} \Delta > 10$.

It is critical that all of the roots up to and including β_{\max} are identified. If a root is missed, energy conservation cannot be satisfied. The steady state case limiting scenario, i.e., q_o'' and t_N are constants, requires the summation of X_o and Y_o to approach the total thermal resistance and unity, respectively. A useful check is to ensure that

$$\sum_{j=0}^{n_x} X_{o,j} = R_{\text{total}} \quad (18)$$

and

$$\sum_{j=0}^{n_y} Y_{o,j} = 1 \quad (19)$$

The wall surface temperature solution for the time of interest θ_n can then be found as

$$t_o(\theta_n) = \sum_{j=0}^{n_x} X_{o,j} \cdot q_o''_{\theta_n - j\Delta} + \sum_{j=0}^{n_y} Y_{o,j} \cdot t_{N,\theta_n - j\Delta} \quad (20)$$

where X_i and Y_i come from Eq. (17). The summation corresponds to the contribution of all previous pulses for both heat flux and backside temperature. Eq. (20) can be seen as the convolution (denoted with \otimes) of the unsteady combustion surface heat flux q_o'' with X_o and the convolution of the coolant surface temperature t_N with Y_o , as

$$t_o(\theta_n) = X_o \otimes q_o'' + Y_o \otimes t_N \quad (21)$$

The convolution can be found quickly using a Fast Fourier Transform (FFT, \mathcal{F}), e.g., $X_o \otimes q_o'' = \mathcal{F}^{-1}\{\mathcal{F}\{X_o\} \cdot \mathcal{F}\{q_o''\}\}$. A computational efficiency comparison to a standard finite difference scheme is given below.

2.4. Initial conditions

Engine walls with large thermal mass, e.g., thick coatings on steel substrates, require a long time for the wall to heat up. Solving a cyclic heat conduction problem solely with the boundary conditions shown in Eqs. (2)–(3) will require a large number of cycles to reach the periodic

converged solution. Finite difference approaches have the same issue. An appropriate initial condition can mitigate this transient period by starting from an approximate steady state condition.

The general solution given in Eq. (21) can be expanded to include initial conditions as

$$t_o(\theta_n) = \bar{q}_o'' \left(R_{\text{total}} - \sum_{j=0}^{n_x} X_{o,j} \right) + X_o \otimes \bar{q}_o'' + t_{N,\text{ini}} \left(1 - \sum_{j=0}^{n_y} Y_{o,j} \right) + Y_o \otimes t_N \quad (22)$$

where \bar{q}_o'' and $t_{N,\text{ini}}$ are the cycle-mean steady state heat flux and initial backside temperature, respectively.

Consider first the heat flux. The term $\bar{q}_o'' R_{\text{total}}$ is the steady surface temperature due to a steady \bar{q}_o'' , but its effect dissipates for $\theta > 0$ as it is replaced by \bar{q}_o'' . The decay rate is given by X_o , and from Eq. (18) one sees that the first term in Eq. (22) goes to zero over time. The effect is analogous for the backside temperature as $(1 - \sum Y_{o,j})$ approaches zero at long times.

3. Interface temperatures

The combustion chamber surface temperature may not be the only temperature of interest. The same approach can be used to find the temperature at any location inside the coated wall.

3.1. Interface temperature subject to unsteady combustion chamber heat flux

Consider the case where an interfacial temperature of a multilayer wall is of interest. Positive heat flow is considered in the direction from the combustion chamber, $x = 0$, to the wall back surface, $x = L$. The interface location of interest splits the problem into two spatial domains. The upstream part starts from the combustion surface and ends at the interface location; the downstream part starts from the interface and ends at the backside surface. Upstream and downstream transfer matrices are shown in Eqs. (23) and (24), where \hat{t}_i and \hat{q}_i are the Laplace transforms of the interface temperature and heat flux.

$$\begin{bmatrix} \hat{t}_o \\ \hat{q}_o \end{bmatrix} = \begin{bmatrix} A_u & B_u \\ C_u & D_u \end{bmatrix} \begin{bmatrix} \hat{t}_i \\ \hat{q}_i \end{bmatrix} \quad (23)$$

$$\begin{bmatrix} \hat{t}_i \\ \hat{q}_i \end{bmatrix} = \begin{bmatrix} A_d & B_d \\ C_d & D_d \end{bmatrix} \begin{bmatrix} \hat{t}_N \\ \hat{q}_N \end{bmatrix} \quad (24)$$

The interface temperature solution can be found from the upstream section by inverting the matrix and using the fact that the determinant is unity for each individual layer and any combination of layers

$$\begin{bmatrix} \hat{t}_i \\ \hat{q}_i \end{bmatrix} = \begin{bmatrix} D_u & -B_u \\ -C_u & A_u \end{bmatrix} \begin{bmatrix} \hat{t}_o \\ \hat{q}_o \end{bmatrix} \quad (25)$$

which relates interface i information to the combustion surface. The interface temperature transform can then be written as

$$\hat{t}_i = D_u \hat{t}_o - B_u \hat{q}_o \quad (26)$$

Assuming \hat{t}_N is zero, Eq. (10) can be used to replace \hat{t}_o and get the interface temperature as exclusively a function of \hat{q}_o .

$$\hat{t}_i = \left(\frac{D_u B - D B_u}{D} \right) \hat{q}_o \quad (27)$$

By multiplying the upstream and downstream matrices one can find

$$B_d = D_u B - D B_u \quad (28)$$

This allows the interface temperature transform \hat{t}_i to be found as

$$\hat{t}_i = \left(\frac{B_d}{D} \right) \cdot \hat{q}_o \quad (29)$$

where B_d and D are the downstream and overall transfer matrix coefficients, respectively. The inversion of Eq. (29) to find interface

temperature t_i , therefore, follows the same procedure as shown in Eq. (17) with $\psi = B_d$ and does not require the effort of finding any other poles.

The interface temperature t_i can be seen as the convolution of surface unsteady combustion surface heat flux \bar{q}_o'' with the interface response function X_i as

$$t_i(\theta_n) = X_i \otimes \bar{q}_o'' \quad (30)$$

3.2. Interface temperature subject to unsteady backside temperature

The interface temperature subject to unsteady backside temperature changes can be solved separately. The problem is formulated as linear, thus, superposition with the previous sub-problem comprises the general solution.

Consider negative heat flow entering the wall from the coolant or oil surface. The “Upstream” and “Downstream” terms were attributed to the positive heat flow direction and that same nomenclature is maintained. The interface temperature can be expressed from Eq. (24)

$$\hat{t}_i = A_d \hat{t}_N + B_d \hat{q}_N \quad (31)$$

by assuming $\hat{q}_o = 0$, Eq. (9) gives $\hat{q}_N = \frac{-C}{D} \hat{t}_N$, which provides the interface temperature exclusively as a function of \hat{t}_N .

$$\hat{t}_i = \frac{A_d D - B_d C}{D} \hat{t}_N \quad (32)$$

By multiplying the upstream and downstream matrices one finds

$$D_u = A_d D - B_d C \quad (33)$$

so the interface temperature \hat{t}_i to be found to be

$$\hat{t}_i = \left(\frac{D_u}{D} \right) \cdot \hat{t}_N \quad (34)$$

where D_u and D are the upstream and overall transfer matrix coefficients, respectively. The inversion of Eq. (34) to find the interface temperature t_i which is the contribution associated with time-varying backside temperature, therefore, again does not require finding new poles and follows the same procedure as Eq. (17) with $\psi = D_u$ giving rise to the transfer function, Y_i . Eq. (34) can be treated in an analogous manner as Eq. (29). Finally, the total interface temperature solution can be found similarly to Eq. (30).

4. Demonstration of the method

An example to illustrate the surface and interface responses X_i and Y_i in a multilayer coated wall is presented to demonstrate application of the method. The thermal properties for each layer can be found in Table 1. This coating architecture can be characterized as a traditional thermal barrier coating for diesel engines [19]. The bond coating increases adhesion to the metal piston and the gradient coating is added to reduce the thermal coefficient of expansion mismatch between coating and substrate to improve durability. The backside of the wall experiences convection with a constant heat transfer coefficient h_{back} . A 120 μs time step was selected for a total simulation time of 0.6 s. By following the above description, 191 poles for a maximum cut-off frequency β_{max} of 134 kHz were used along the negative real-axis.

Fig. 4(a) shows the response functions X_i for all of the interfaces of this coating structure. The negative time on the plot abscissa emphasizes the fact that *past* heat flux pulses are contributing to the *current* wall temperature. The surface (solid) and interface (dashed) time-response functions X assume a heat flux change of unity at the combustion chamber surface while the coolant or oil surface temperature is fixed. The surface response starts at a high value because it is directly exposed to the applied heat flux, then attenuates rapidly. The interface response functions start at zero due to the finite time required for the thermal wave to reach the interior locations, then peak in sequence according to their depth.

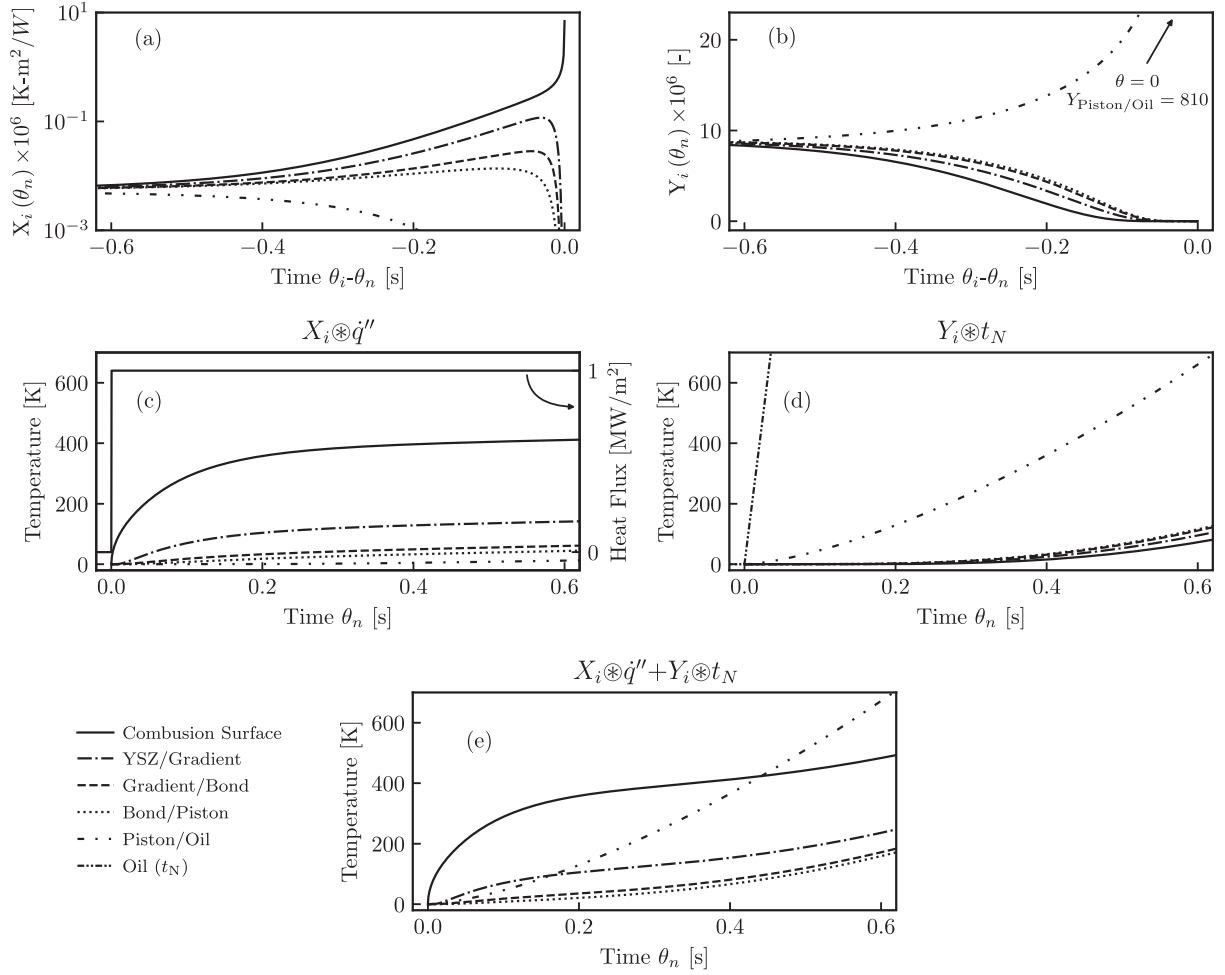


Fig. 4. Surface and interface time response functions (a) X_i and (b) Y_i are shown for a multilayer thermal barrier coating on an engine piston. (c) The temperature at the interfaces due to time-varying heat flux at the combustion chamber surface, \dot{q}'' , and (d) time-varying temperature at the backside surface, t_N . (e) The combined effect of both boundary conditions. See text for additional information about thermal properties and thicknesses.

The X_i shown in Fig. 4(a) can be used to generate temperature histories given the surface heat flux. For this demonstration, a step change in heat flux from 0 to 1 MW/m² was taken. The resulting surface and interface temperatures are shown in Fig. 4(c). The oil temperature was maintained fixed at 430 K and initial condition was neglected, i.e. $\dot{q}'' = 0$ for $\theta < 0$. The higher surface temperature is mainly due to the low thermal conductivity of the top coat. It serves as thermal insulator for the rest of the multilayer engine wall.

The same multilayer architecture was used to illustrate the surface and interface response functions, Y_i , which are shown in Fig. 4(b). These time-response Y functions were convolved with a linear temperature change at the backside surface, as shown in Fig. 4(d), while the combustion surface heat flux was maintained at zero. The convection heat transfer resistance is high and accounts for the big difference between oil and backside wall temperature. Lastly, the combined effect of Fig. 4(c) and (d) is depicted in Fig. 4(e). The surface and interface temperatures illustrate the superpositioned of a heat flux change at the combustion surface and a temperature change at the backside surface.

5. Computational speed and accuracy comparison

5.1. Comparison with finite difference scheme

A surrogate of the in-cylinder heat flux profile was developed as the sum of a sinusoidal function with a period that corresponds to one engine cycle at 1300 rpm and a Gaussian pulse to represent the

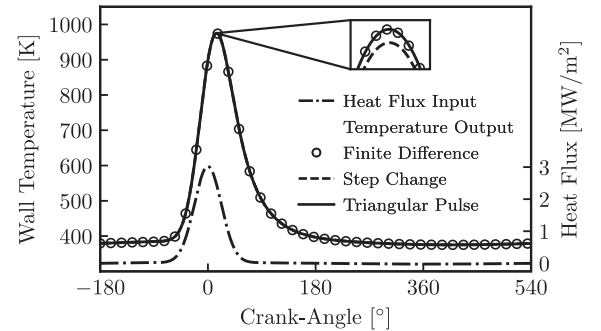


Fig. 5. Crank-resolved surface temperature of a two-layer engine wall subject to the unsteady surface heat flux shown with dash-dot line and right axis. The finite difference (circles), step change (dashed), and proposed triangular pulse method (solid) surface temperatures provide excellent agreement. Material properties can be found in [12].

combustion event. The applied heat flux is shown in Fig. 5, as a function of crank angle. The Gaussian term had a peak heat flux of 3 MW/m² and a full-width at half-maximum value of 5.1 ms. The sinusoidal term, which had an amplitude of 0.25 MW/m², modeled the background heat flux due to the reciprocating piston motion [12].

A two-layer wall was considered with Layer 1 being a 100 μ m thermal insulation coating and Layer 2 an aluminum wall; the total domain length was 5 mm. The backside temperature was steady at 373

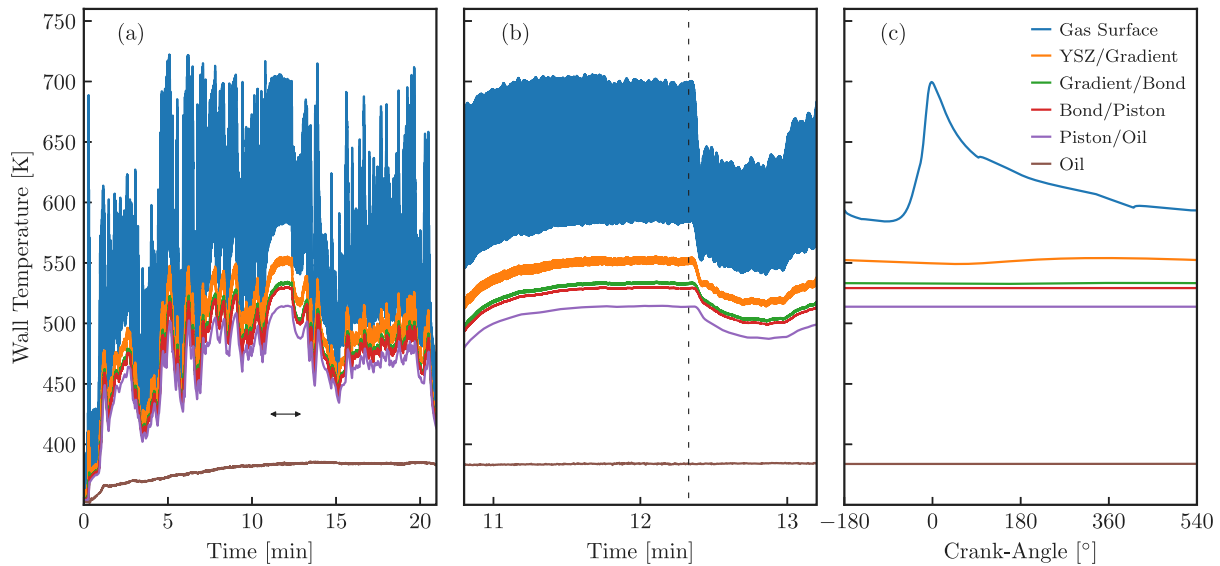


Fig. 6. Temperature histories of a multilayer coated engine wall for: (a) full drive, (b) magnified 11th–13th minute window indicated by the horizontal arrow in (a), and (c) individual cycle indicated by the vertical dashed line of (b). Details about the boundary conditions can be found in [11].

Table 1

Thermo-mechanical properties of wall architectures investigated, with k : thermal conductivity; ρ : density; c : specific heat capacity; L : thickness; and h_{back} heat transfer coefficient on the backside surface.

Material	k [W/m-K]	ρ [kg/m ³]	c [J/kg-K]	L [μm]	h_{back} [W/m ² -K]
YSZ	0.77	4713	387.5	210	–
Gradient	0.85	3886	385.1	70	–
Bond	4.07	6255	152.6	70	–
Aluminum piston	123	2702	949	8250	–
Oil	–	–	–	–	1750

K. The cycle-averaged heat flux \bar{q}'' of the profile was used as the initial condition.

Fig. 5 shows the surface temperature output for: a high resolution finite difference solution, the step change method based on our previous publication [12], and the current triangular pulse method. The finite difference solution used a Crank–Nicolson scheme with 2^{20} nodes divided evenly between the coating and substrate. The simulation time step was 2^{19} , 2^{16} and 2^{16} for the finite difference and the step, and triangular solutions, respectively. The finite difference was considered as the reference or “exact” solution. The triangular pulse (solid) was resolved using Eq. (22). The step and triangular pulse methods were compared for a fixed number (70) of roots.

All three techniques show excellent agreement, however, the step change solution has a small error (0.02 K) in peak wall temperature as shown in the expanded view of Fig. 5.

Fig. 7(a) shows the computational time versus maximum error for each of the aforementioned methods. The maximum error was based on the “exact” finite difference scheme, discussed above. Only two cycles were simulated and the maximum error was calculated for just the second cycle to avoid initial transient errors. The CPU time shown was for both cycles. The three methods were evaluated for different numbers of time steps ranging from 2^5 to 2^{16} , in multiplicative steps of two. The finite difference results are shown as a family of dashed curves; each individual curve represents a fixed number of spatial nodes calculated for using the different time step sizes.

Consider the finite difference solution with 2^{11} nodes. The lower right-most point corresponds to 2^5 time steps, and the upper left-most point corresponds to 2^{16} time steps. As the error decreases with increased number of time steps, the computational time increases proportionally. Finally, a condition is reached where the errors of spatial

discretization dominate, and the curve becomes vertical. This pattern is seen for all but 2^4 and 2^5 spatial nodes, which are solely vertical due to the low spatial resolution.

The step response and triangular pulse analytical techniques were evaluated using a common computational approach and thus took the same CPU time, but they vary substantially in accuracy. The convolution was calculated via Fast Fourier Transform (FFT), see Eq. (21), using the entire heat flux history, i.e., in a single step. The FFT convolution offers substantial computational speed improvement relative to the direct form convolution approach in Eq. (20).

The analytical step-response method showed significant speed advantage relative to the finite difference cases, however, the accuracy was limited to ~ 0.1 K maximum error. The accuracy of this method would have been improved if the time step was reduced, but this is impractical. The limited accuracy stems from the poor representation of the step change to the continuous input function, as shown in Fig. 2.

The current triangular pulse approximation, which fits the continuous input function better in Fig. 2, gives the best performance in Fig. 7(a). The triangular pulse offers two to three orders of magnitude reduction in computational time compared with the finite difference approach at similar error levels. In addition, the error is much smaller relative to the step change, which requires the same computational effort.

5.2. Engine drive cycle demonstration

Computing component temperatures during long engine transients, e.g., cold starts or drive cycles, is of interest. Thermodynamic and heat transfer analysis was performed on a production John Deere 4045 diesel engine using the commercial simulation code GT-Power augmented with the wall temperature solver using the triangular pulse method, see [11]. All major subsystems in this model used either bench data or were suitably calibrated, including the head flow, EGR valve, exhaust throttle, turbocharger, wastegate, fuel rate of injection profiles, and combustion parameters. The Non-Road Transient Cycle (NRTC) is an international transient certification cycle used to assess non-road engine vehicle performance, fuel consumption and emissions. The cycle lasts about 20 min; official certification involves running an NRTC from cold start, followed by a 20-min soak period, and finally an NRTC from hot start. The hot NRTC is used to evaluate performance and fuel consumption. The drive cycle was run experimentally and the data were recorded to be used as boundary conditions. The measured

oil temperature history was used to set the backside time-varying temperature. Further details on the system-level analysis can be seen in [11].

The piston heat flux and backside temperature histories were exported from the model results and used as time-varying boundary conditions. The initial conditions were set at 0 MW/m² and 353 K (80 °C) for the combustion chamber and oil temperature, respectively. The same multilayer coating discussed in Table 1 was utilized for this example. All temperature histories were computed using Eq. (22).

Fig. 6(a) shows the temperature histories at all interfaces in the coated piston during the full drive cycle. The surface wall temperature shows two differences relative to the other interfaces. First, it reaches significantly higher temperatures due to the low conductivity of the top coat. Second, the low-volumetric heat capacity of the top coat causes the surface temperature to respond quickly to the heat flux changes. The measured oil temperature history, used as boundary condition, is shown as a reference. Fig. 6(b) shows a magnified time. Shortly after the vertical dashed line location, the engine experiences a sudden load decrease [11]. This has an immediate effect on the engine heat transfer; all the temperatures decrease. In addition, the vertical dashed line also indicates the engine cycle shown in Fig. 6(c). This cycle generated a relatively high instantaneous surface temperature. The intra-cycle interface temperature variations are minor progressing from top coat to the aluminum piston. The YSZ/Gradient interface has an intra-cycle temperature swing of only 5 K.

Fig. 7(b) shows a comparison between the CPU time and the cumulative simulated real time for three different computational approaches. A maximum error threshold of 10⁻¹ K was selected for the finite difference case, and from Fig. 7(a), this level of error can be achieved by using 2⁷ and 2⁶ nodes in the coating and substrate, respectively, for peak computational efficiency. The other two results are based on the triangular pulse analytical solution proposed in this work. The Single Block FFT computes the convolution using an FFT similar to the procedure followed in Fig. 7(a). A constant ratio in computational time was realized; the Single Block FFT was more than 10²× faster compared to the finite difference case. On top of this benefit, additional computational performance can be achieved with an advanced convolution treatment. The Overlap-add FFT method is used to decompose long signals into smaller segments for easier digital signal processing [20]. In this Overlap-Add algorithm application, the heat flux \dot{q}'' is the very long signal and the response function X_o is the finite-impulse-response filter. The Overlap-add FFT approach provided more than a 10⁴× speed increase relative to the finite difference equivalent. In particular, the CPU time of a full drive cycle reduced from about 3105 s to less than 0.25 s

6. Frequency response characterization

The fact that the wall response function is convolved with the applied heat flux to find surface temperature suggests that the system can be modeled as a filter or transfer function. The function $X(\theta)$ is analogous to the finite impulse response. It is also instructive to study the transfer function in the frequency domain, which can be found by taking the power spectral density of X .

The frequency response can also be directly evaluated. Consider the case where the backside temperature is fixed, $\hat{i}_N = 0$, and the combustion surface heat flux is varying periodically, $\dot{q}''_o(\theta) = \sin(\omega\theta)$, where $\omega = 2\pi f$ is angular velocity and f is frequency. The system transfer function in the Laplace domain, i.e. the temperature response to a heat flux input, is given by \hat{i}_o/\hat{q}_o

$$\frac{\hat{i}_o}{\hat{q}_o} = \frac{B}{D} \quad (35)$$

One can convert from the Laplace to the Fourier frequency domain using $s = j\omega$. In the case of a single sinusoidal input at ω , the inversion to the time domain simply gives

$$|\hat{X}_o(j\omega)| = \left| \frac{B(j\omega)}{D(j\omega)} \right| \quad (36)$$

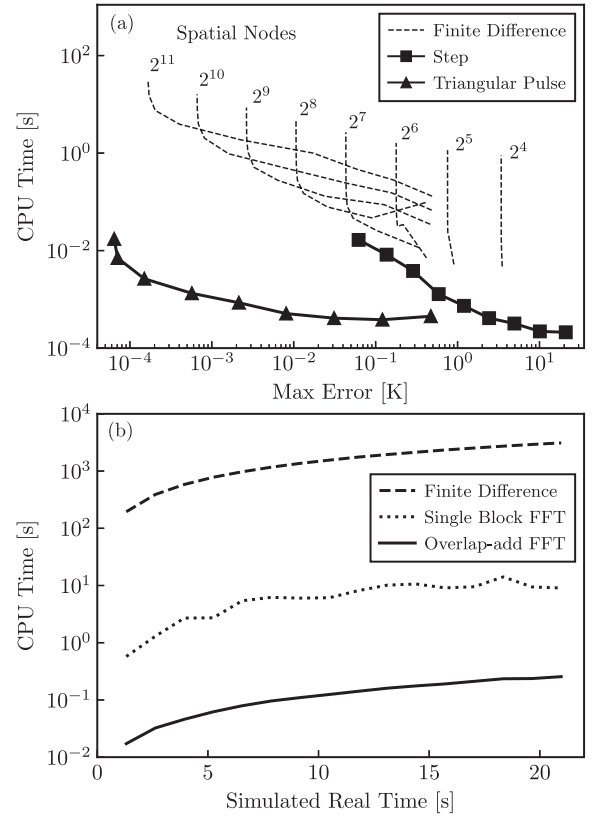


Fig. 7. (a) Computational time and maximum surface temperature error for different solution methods. Finite Difference (dashed) curves refer to simulations with varying time step and the total number of grid points shown. The analytical techniques of step change (solid square) and triangular pulse (solid triangle) are solved using the FFT method for different time step sizes. For further details, see text. (b) Comparison between computational time and simulated real time for 2⁸-node finite difference, single block FFT, and Overlap-add FFT solution methods.

where $|\hat{X}_o(j\omega)|$ is the magnitude of the complex function $\frac{B}{D}$. The magnitude, which is of primary interest instead of the phase, determines the relative temperature response to an applied heat flux. The system response magnitude in Eq. (36) can be viewed in the frequency domain to distinguish the dynamics of different coating structures.

Consider the example of an uncoated and coated aluminum wall with thermal properties shown in Table 1, excluding the oil layer. Fig. 8(a) shows the surface response, X_o [K-m²/W], in the time domain. Note, these results are nearly identical to Fig. 4(a) except that the time axis is not reversed and a logarithmic abscissa is used. There is a significant difference between the uncoated and coated wall at short times, which is intuitive for a thermal-swing coating as was chosen for this example. At long times, however, the response of the different wall types is indistinguishable. In fact, the time constant for the YSZ coating, $\tau = RC$, is 0.1 s, which is shown with the vertical dashed line in Fig. 8(a). This time scale is found to define the transition from coating-dominated performance well. For times longer than τ the layer with the longest time scale, usually the substrate, dominates.

Fig. 8(b) illustrates the coated and uncoated magnitude of surface response, $|\hat{X}_o(j\omega)|$ [K-m²/W-Hz] in the frequency domain, which gives a complementary view to the time-domain response. The value of the magnitude at the lowest frequency is representative of the steady state resistance of the wall. This is made clear by the way that the temperature response at a given frequency is calculated

$$\hat{i}_o(j\omega) = \hat{X}_o(j\omega) \cdot \hat{q}_o(j\omega) \quad (37)$$

is simply the product of the “effective” resistance and the applied heat flux at that frequency. For all frequencies, the coated wall has a higher

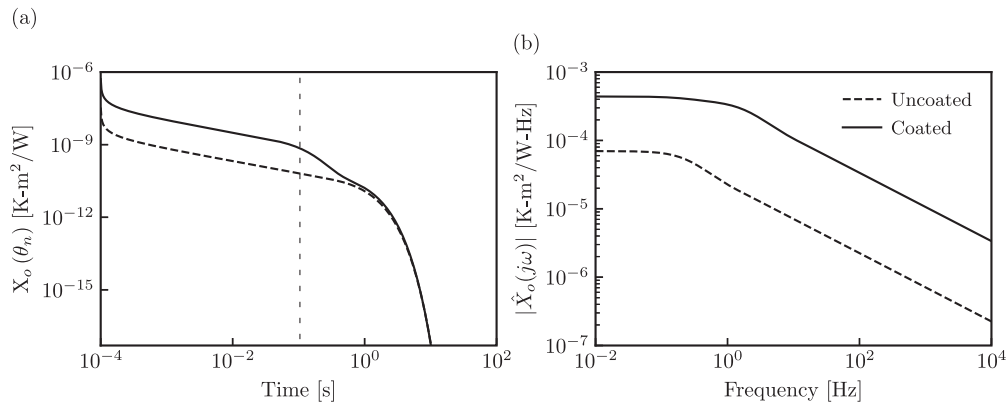


Fig. 8. (a) Time- and (b) Frequency surface response X_o for an uncoated and coated engine wall.

response than the uncoated wall. As expected, the response of the wall to an applied heat flux decreases as the frequency increases. At low frequencies, the coated wall has higher steady response, or thermal insulation ability, which was not apparent in the time domain plot. At high frequencies, the coated wall surface has increased ability to follow the gas temperature transients, a desirable attribute for a thermal-swing coating.

Fig. 9 compares a number of coatings in the frequency domain. The different colors represent coating architecture, and correspond roughly to periods of reciprocating engine coatings research. Engine performance is improved by coatings capable of delivering (i) higher insulation ability at steady response, and (ii) increased surface temperature swings at high frequencies. Thus, curves in the upper right-hand corner represent the best performance.

Thermal properties for all the coatings in Fig. 9 are given in Table B.2. The blue curve represents an aluminum baseline, which was used as the substrate for all the cases except #1 and #2. The orange family of curves (#1-4) represent single- and multi-layer monolithic ceramic engine walls (#1 and #2), air-gapped pistons (#3), and thick thermal barrier coatings adapted from the gas-turbine industry (#4), which were investigated during the 1980s and 1990s. The green family of curves (#5-8) represent modern coatings, demonstrated during the 2010s, using alternative materials with lower volumetric heat capacity. The red curves (#9-10) represent two potential coating materials (silica aerogel and carbon foam) that emerged from a large-scale thermo-mechanical optimization study over a full drive cycle; see [21] for further details. It is worth emphasizing that there is more than an order of magnitude opportunity for improvement, both in the low- and high-frequency region, possible based on the results of [21], although these materials have yet to be applied in a real-world application.

7. Summary and conclusions

Unsteady heat conduction in multilayer walls was investigated analytically under the assumption of one-dimensional heat flow. Time-varying heat flux and temperature boundary conditions were applied to the domain. This approach can be applied to a number of applications, but the specific problem of interest was thermal barrier coatings applied to the surfaces of reciprocating internal combustion engines.

The matrix method coupled with complex analysis for Laplace transform inversion was used to analyze the problem. The boundary conditions were approximated as a unit-magnitude triangular pulse; the superposition of adjacent pulses in the time domain provides a piece-wise linear approximation of the applied heat flux or backside temperature profile. The temperature at any interface is found as the discrete-time convolution of the heat flux or backside temperature time history with a transfer function, X_i or Y_i , respectively, where the subscript i denotes the interface of interest. The transfer functions

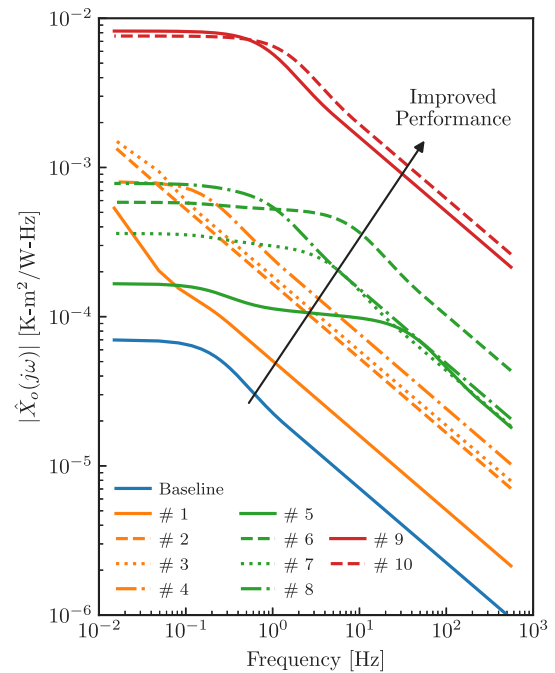


Fig. 9. Surface response, X_o , for various coatings from the reciprocating engine literature. Table B.2 gives properties of each coating and their original references. The arrow indicates the direction of the improved performance. The baseline, historic, modern and advanced walls are shown in blue, orange, green, and red, respectively.

describe the exact heat transfer response and only depends on material properties and geometry, therefore, they can be computed *a priori*.

This method provides paramount computational efficiency while guaranteeing the accuracy of an analytical solution. At a fixed level of accuracy, it was at least two orders of magnitude faster than a finite difference scheme. The discrete triangular pulse approximated the continuous input boundary condition with substantially higher accuracy than the step-change method from a previous publication by the same authors; the computational time is the same, but accuracy is two to three orders of magnitude better. Applying this method to long drive cycles, and using the Overlap-add FFT, the computational times were up to four orders of magnitude shorter than a finite difference method at matched temperature accuracy.

Investigation of the wall response functions in the frequency domain reveal complementary information to the time domain. At low frequencies, the thermal insulation ability difference between an uncoated and coated wall was indistinguishable in the time domain, but shows a clear difference in the frequency domain, consistent with coated

cases having lower net heat transfer. A comparison between various coating architectures from the reciprocating engine literature showed the improvement in thermal performance of coatings with development time, and highlighted the potential for future improvements.

Acknowledgments

Support for this work was provided by Deere & Company.

Appendix A. Evaluation of transfer matrix and its derivative

The transfer matrix and its derivative with respect to the frequency variable are necessary to calculate the inverse Laplace transform exactly. The matrix describing layer i is

$$[M_i] = \begin{bmatrix} A_i(s) & B_i(s) \\ C_i(s) & D_i(s) \end{bmatrix} \quad (\text{A.1})$$

and the overall matrix, consisting of N layers, is

$$[M] = \prod_{i=1}^N [M_i] \quad (\text{A.2})$$

It is convenient to set $s = -\beta_m$ for root-calculating purposes so that β becomes a positive real number. Invoking the assumption that the poles lie on the negative real axis [13], M_i can be written as

$$[M_i] = \begin{bmatrix} A_i & B_i \\ C_i & D_i \end{bmatrix} = \begin{bmatrix} \cos \sqrt{\beta} R_i C_i & \frac{R_i}{\sqrt{\beta} R_i C_i} \sin \sqrt{\beta} R_i C_i \\ -\frac{\sqrt{\beta} R_i C_i}{R_i} \sin \sqrt{\beta} R_i C_i & \cos \sqrt{\beta} R_i C_i \end{bmatrix} \quad (\text{A.3})$$

The derivative of M_i is simply

$$\frac{d}{ds} [M_i] = \begin{bmatrix} \frac{d}{ds} A_i & \frac{d}{ds} B_i \\ \frac{d}{ds} C_i & \frac{d}{ds} D_i \end{bmatrix} \quad (\text{A.4})$$

and by setting $s = -\beta_m$, the matrix derivative becomes

$$\left[\frac{dM_i}{ds} \right] = \frac{R_i C_i}{2} \times \begin{bmatrix} \frac{\sin \sqrt{\beta_m} R_i C_i}{\sqrt{\beta_m} R_i C_i} & \frac{1}{\beta_m C_i} \left\{ \frac{\sin \sqrt{\beta_m} R_i C_i}{\sqrt{\beta_m} R_i C_i} - \cos \sqrt{\beta_m} R_i C_i \right\} \\ \frac{1}{R_i} \left\{ \frac{\sin \sqrt{\beta_m} R_i C_i}{\sqrt{\beta_m} R_i C_i} + \cos \sqrt{\beta_m} R_i C_i \right\} & \frac{\sin \sqrt{\beta_m} R_i C_i}{\sqrt{\beta_m} R_i C_i} \end{bmatrix} \quad (\text{A.5})$$

For the pole at $s = 0$ one should use

$$[M_i]_{s=0} = \begin{bmatrix} 1 & R_i \\ 0 & 1 \end{bmatrix} \quad (\text{A.6})$$

$$\left[\frac{dM_i}{ds} \right]_{s=0} = \frac{R_i C_i}{2} \begin{bmatrix} 1 & R_i/3 \\ 2/R_i & 1 \end{bmatrix} \quad (\text{A.7})$$

which results from the limit $s \rightarrow 0$.

An air layer with negligible heat capacity to model a convective boundary condition on the backside would lead to

$$[M_i]_{s=0} = \begin{bmatrix} 1 & 1/h \\ 0 & 1 \end{bmatrix} \quad (\text{A.8})$$

where h is the convective heat transfer coefficient. All the elements of the transfer matrix derivative of this layer would be zero.

When more than one layer is considered, the overall matrix derivative should be calculated by applying the chain rule as follows:

$$\begin{aligned} \left[\frac{dM}{ds} \right] &= \begin{bmatrix} \frac{dA}{ds} & \frac{dB}{ds} \\ \frac{dC}{ds} & \frac{dD}{ds} \end{bmatrix} = \begin{bmatrix} \frac{dA_1}{ds} & \frac{dB_1}{ds} \\ \frac{dC_1}{ds} & \frac{dD_1}{ds} \end{bmatrix} \cdot \begin{bmatrix} A_2 & B_2 \\ C_2 & D_2 \end{bmatrix} \cdots \begin{bmatrix} A_N & B_N \\ C_N & D_N \end{bmatrix} \\ &+ \begin{bmatrix} A_1 & B_1 \\ C_1 & D_1 \end{bmatrix} \cdot \begin{bmatrix} \frac{dA_2}{ds} & \frac{dB_2}{ds} \\ \frac{dC_2}{ds} & \frac{dD_2}{ds} \end{bmatrix} \cdots \begin{bmatrix} A_N & B_N \\ C_N & D_N \end{bmatrix} \\ &+ \cdots + \begin{bmatrix} A_1 & B_1 \\ C_1 & D_1 \end{bmatrix} \cdot \begin{bmatrix} A_2 & B_2 \\ C_2 & D_2 \end{bmatrix} \cdots \begin{bmatrix} \frac{dA_N}{ds} & \frac{dB_N}{ds} \\ \frac{dC_N}{ds} & \frac{dD_N}{ds} \end{bmatrix} \quad (\text{A.9}) \end{aligned}$$

Table B.2

Thermal properties of wall architectures investigated, with k : thermal conductivity, ρ : density, c : specific heat capacity, and L : thickness.

Wall	Layer	k [W/m-K]	$\rho c \times 10^{-6}$ [J/m ³ -K]	L [μm]
Baseline	Aluminum	123	2.56	8600
#1, Ref. [22]	PSZ	2.5	2.3	10 000
#2, Ref. [23]	PSZ	0.97	2.81	650
	MCrAlY	2.1	4.93	50
	Ti	13.5	2.6	250
	Braze	24.5	5.22	50
	Si3N4	22.5	2.22	2000
#3, Ref. [24]	Nimonic 80A	15.25	4.11	5000
	Air-gap	0.044	0	2000
	Aluminum	123	2.56	5000
#4, Ref. [25]	PSZ	0.67	1.3	65
	Aluminum	123	2.56	6600
#5, Ref. [26]	Sample E	0.42	1.6	300
	Aluminum	123	2.56	8300
#6, Ref. [27]	SPC	0.31	0.49	160
	Aluminum	123	2.56	8440
#7, Ref. [28]	GdZr-SP	0.65	1.3	180
	NiCoCrAlY	4.2	3.08	70
	Aluminum	123	2.56	8350
#8, Ref. [29–31]	SiRPA	0.67	1.3	65
	Aluminum	123	2.56	8535
#9, Ref. [21]	Silica aerogel	0.061	0.1	500
	Aluminum	123	2.56	8100
#10, Ref. [21]	Carbon Foam	0.066	0.063	5000
	Aluminum	123	2.56	8100

or in a compact notation the overall matrix derivative can be described as

$$\left[\frac{dM}{ds} \right] = \sum_{i=0}^{N-1} \left\{ \left[\prod_{j=0}^{i-1} [M_j] \right] \cdot \left[\frac{dM_i}{ds} \right] \cdot \left[\prod_{j=i+1}^{N-1} [M_j] \right] \right\} \quad (\text{A.10})$$

Appendix B. Material properties

See Table B.2.

References

- [1] N. Uchida, A review of thermal barrier coatings for improvement in thermal efficiency of both gasoline and diesel reciprocating engines, *Int. J. Engine Res.* (2020) <http://dx.doi.org/10.1177/1468087420978016>.
- [2] D.N. Assanis, *A Computer Simulation of The Turbocharged Diesel Engine System.pdf*, (Ph.D. thesis), MIT, 1985.
- [3] Y. Miyairi, Computer simulation of an LHR DI diesel engine, 1988, <http://dx.doi.org/10.4271/880187>.
- [4] P. Andruskiewicz, P. Najt, R. Durrett, S. Biesboer, T. Schaedler, R. Payri, Analysis of the effects of wall temperature swing on reciprocating internal combustion engine processes, *Int. J. Engine Res.* (2017) <http://dx.doi.org/10.1177/1468087417717903>.
- [5] T. Morel, R. Keribar, P.N. Blumberg, Cyclical thermal phenomena in engine combustion chamber surfaces, *SAE Tech. Paper Ser.* (1985) <http://dx.doi.org/10.4271/850360>.
- [6] Gamma Technologies, *GT-SUITE*, Westmont, IL, 2020.
- [7] K.J. Richards, P.K. Senecal, E. Pomraning, *CONVERGE 3.0 Manual*, Convergent Science, Madison, WI, USA, 2021.
- [8] P. Olmeda, X. Margot, P. Quintero, J. Escalona, Numerical approach to define a thermodynamically equivalent material for the conjugate heat transfer simulation of very thin coating layers, *Int. J. Heat Mass Transfer* 162 (2020) 120377.
- [9] J. Ghandhi, G. Koutsakis, Comment on “numerical approach to define a thermodynamically equivalent material for the conjugate heat transfer simulation of very thin coating layers” by olmeda, p. and margot, x. and quintero, p. and escalona, j., *Int. J. Heat Mass Transfer* 162 (2020) 120377; *International Journal of Heat and Mass Transfer* 173 (2021) 121190, <http://dx.doi.org/10.1016/j.ijheatmasstransfer.2021.121190>.

- [10] P. Olmeda, X. Margot, P. Quintero, J. Escalona, Reply to short communication ‘Comment on “Numerical approach to define a thermodynamically equivalent material for the conjugate heat transfer simulation of very thin coating layers” by olmeda, p. and margot, x. and quintero, p. and escalona, j, Int. J. Heat Mass Transfer 162 (2020) 120377, by Jaal Ghandhi and Georgios Koutsakis; International Journal of Heat and Mass Transfer 171 (2021) 121023, <http://dx.doi.org/10.1016/j.ijheatmasstransfer.2021.121023>.
- [11] G. Koutsakis, S. Miles, J. Ghandhi, Assessment of in-cylinder thermal barrier coatings over a full vehicle drive cycle, SAE Int. (2021) <http://dx.doi.org/10.4271/2021-01-0456>.
- [12] G. Koutsakis, G.F. Nellis, J.B. Ghandhi, Surface temperature of a multi-layer thermal barrier coated wall subject to an unsteady heat flux, Int. J. Heat Mass Transfer 155 (2020) <http://dx.doi.org/10.1016/j.ijheatmasstransfer.2020.119645>.
- [13] H. Carslaw, J. Jaeger, Conduction of heat in solids, 1959, <http://dx.doi.org/10.1371/journal.pone.0041178>.
- [14] D.G. Stephenson, G. Mitalas, Calculation of heat conduction transfer functions for multi-layers slabs, Air Cond. Engrs. Trans 77 (1971).
- [15] D.C. Hittle, Calculating Building Heating and Cooling Loads Using the Frequency Response of Multilayered Slabs, Tech. rep, Construction Engineering Research Lab (ARMY) Champaign-IL, 1981.
- [16] T. Kusuda, Thermal response factors for multi-layer structures of various heat conduction systems, in: Ashrae Journal, Vol. 11, 1969, p. 64.
- [17] L.A. Pipes, Matrix analysis of heat transfer problems, J. Franklin Inst. B 263 (3) (1957) 195–206.
- [18] R.V. Churchill, J.W. Brown, Complex Variables and Applications, eighth ed, McGraw-Hill, 2009.
- [19] E. Gingrich, M. Tess, V. Korivi, P. Schihl, J. Saputo, G.M. Smith, S. Sampath, J. Ghandhi, The impact of piston thermal barrier coating roughness on high-load diesel operation, Int. J. Engine Res. (2019) <http://dx.doi.org/10.1177/1468087419893487>.
- [20] L.R. Rabiner, B. Gold, Theory and Application of Digital Signal Processing, Englewood Cliffs: Prentice-Hall, 1975, pp. 63–65.
- [21] G. Koutsakis, J.B. Ghandhi, Optimization of thermal barrier coating performance and durability over a drive cycle, Int. J. Engine Res. (2022) <http://dx.doi.org/10.1177/14680874221089072>.
- [22] R. Keribar, T. Morel, Thermal shock calculations in IC engines, SAE Trans. (1987) 130–148.
- [23] L. Kamo, M. Woods, W. Bryzik, M. Mekari, Thermal barrier coatings for monolithic ceramic low heat rejection diesel engine components, SAE Trans. (2000) 681–690.
- [24] G. Woschni, W. Spindler, K. Kolesa, Heat insulation of combustion chamber walls—a measure to decrease the fuel consumption of IC engines? SAE Trans. (1987) 269–279, URL <https://www.jstor.org/stable/44470841>.
- [25] D.N. Assanis, E. Badillo, Transient analysis of piston-liner heat transfer in low-heat-rejection diesel engines, SAE Trans. 97 (1988) 295–305, URL <http://www.jstor.org/stable/44547375>.
- [26] J.C. Saputo, G.M. Smith, H. Lee, S. Sampath, E. Gingrich, M. Tess, Thermal swing evaluation of thermal barrier coatings for diesel engines, J. Therm. Spray Technol. (2021) 1–15, <http://dx.doi.org/10.1007/s11666-020-01117-3>.
- [27] A. Babu, G. Koutsakis, S. Kokjohn, M. Andrie, Experimental and analytical study of temperature swing piston coatings in a medium-duty diesel engine, SAE Techn. Paper (2022) <http://dx.doi.org/10.4271/2022-01-0442>.
- [28] Z. Filipi, M. Hoffman, R. O'Donnell, T. Powell, E. Jordan, R. Kumar, Enhancing the efficiency benefit of thermal barrier coatings for homogeneous charge compression ignition engines through application of a low-k oxide, Int. J. Engine Res. (2020) <http://dx.doi.org/10.1177/1468087420918406>.
- [29] H. Kosaka, Y. Wakisaka, Y. Nomura, Y. Hotta, M. Koike, K. Nakakita, A. Kawaguchi, Concept of “temperature swing heat insulation” in combustion chamber walls, and appropriate thermo-physical properties for heat insulation coat, SAE Int. J. Engines 6 (1) (2013) 142–149, <http://dx.doi.org/10.4271/2013-01-0274>.
- [30] Y. Wakisaka, M. Inayoshi, K. Fukui, H. Kosaka, Y. Hotta, A. Kawaguchi, N. Takada, Reduction of heat loss and improvement of thermal efficiency by application of “Temperature Swing” insulation to direct-injection diesel engines, SAE Int. J. Engines 9 (3) (2016) 1449–1459, <http://dx.doi.org/10.4271/2016-01-0661>.
- [31] A. Kawaguchi, Y. Wakisaka, N. Nishikawa, H. Kosaka, H. Yamashita, C. Yamashita, H. Iguma, K. Fukui, N. Takada, T. Tomoda, Thermo-swing insulation to reduce heat loss from the combustion chamber wall of a diesel engine, Int. J. Engine Res. (2019) <http://dx.doi.org/10.1177/1468087419852013>.